Optics & Laser Technology 181 (2025) 111799

Contents lists available at ScienceDirect

Optics and Laser Technology

journal homepage: www.elsevier.com/locate/optlastec

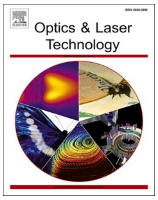

Full length article

Local laser annealing for amorphous/polycrystalline silicon hybrid photonics on CMOS

Junying Li [a,*,1], Lichun Wang [b,1], Xinru Xu [c,1], Kunhao Lei [b], Bo Tang [d], Hao Dai [b], Jiaxin Zhang [a], Jialing Jian [e], Yuting Ye [e], Hui Ma [b], Jianghong Wu [e], Ye Luo [e], Zequn Chen [e], Yuexin Yin [c], Chunlei Sun [e], Daming Zhang [c,*], Lan Li [e], Hongtao Lin [b,*]

[a] Hangzhou Institute for Advanced Study, University of Chinese Academy of Sciences, Hangzhou 310024, China
[b] State Key Lab of Brain-Machine Intelligence, Key Laboratory of Micro-Nano Electronics and Smart System of Zhejiang Province, College of Information Science and Electronic Engineering, Zhejiang University, Hangzhou 310027, China
[c] State Key Laboratory of Integrated Optoelectronics, College of Electronic Science and Engineering, Jilin University, Changchun 130012, China
[d] Institute of Microelectronics of the Chinese Academy of Sciences, Beijing, 100029, China
[e] Key Laboratory of 3D Micro/Nano Fabrication and Characterization of Zhejiang Province, School of Engineering, Westlake University, Hangzhou, Zhejiang 310030, China

ARTICLE INFO

Keywords:
Laser annealing
Silicon photonics
Amorphous silicon
Polycrystalline silicon

ABSTRACT

Deposited photonics represents a promising avenue for monolithic back-end integration on CMOS, yet encounters challenges in simultaneously enhancing waveguide loss and modulation dynamics. In this paper, a novel amorphous/polycrystalline hybrid scheme for deposited silicon photonics on CMOS was proposed, which utilizes mask-assisted local laser annealing to crystallize the active region of low-loss amorphous silicon (α-Si) PICs only into high-mobility polycrystalline silicon (poly-Si). The feasibility of key techniques such as laser annealing of α-Si thin films, laser activation of doping ions, and mask-assisted local laser annealing of photonic devices is validated. A comparative study between excimer laser annealing and solid-state laser annealing of α-Si is conducted, examining the impacts of pre-dehydrogenation, doping, etching depth, laser pulse energy density, and pulse number. During mask-assisted laser annealing the necessity of a buffer layer between the mask and the α-Si to prevent metal contamination is highlighted. The mask-assisted local laser annealing technique effectively mitigates the optical loss increase by ~140 dB/cm typically associated with laser crystallization in a α-Si racetrack resonator and reduces the coupling loss in grating couplers by ~8 dB/pair. Mask-assisted laser annealing not only facilitates high-yield wafer-level active deposited photonics but also allows for leveraging the strengths of both α-Si and poly-Si within a single photonic integrated circuit. This work provides technological insights and valuable guidance for the development of high-performance deposited silicon photonics.

1. Introduction

Over the past decades, significant progress has been made in silicon photonics, driven by silicon's excellent optoelectronic properties and mature semiconductor fabrication techniques [1]. Silicon-based photonic integrated circuits (PICs) have already achieved commercial success in optical communications [2] and hold promising applications in LiDAR [3], photonic computing [4], programmable networks [5], and sensing [6]. An ideal optoelectronic integration system envisions the monolithic integration of PICs with CMOS microelectronics [7] to minimize parasitic capacitance between electronic and photonic devices, achieving ultra-low power consumption, latency, and complexity. A combined front-end process [8–11], which mixes electronics and photonics process steps, has achieved high-performance monolithic integrated systems. However, due to the lack of the thick optical isolation layer needed for waveguides in CMOS processing, as well as the much larger size of photonic devices compared to transistors, the combined front-end technique is not only complex but may also potentially result in inefficient use of advanced nodes. It is more flexible to fabricate PICs directly on the mature CMOS chips using decoupled processes, but the

---

* Corresponding authors.
E-mail addresses: junyingli@ucas.ac.cn (J. Li), zhangdm@jlu.edu.cn (D. Zhang), hometown@zju.edu.cn (H. Lin).
[1] Authors contributed equally.

https://doi.org/10.1016/j.optlastec.2024.111799
Received 24 June 2024; Received in revised form 17 August 2024; Accepted 11 September 2024

monolithic back-end integration of photonics on CMOS chips requires a thermal budget lower than ~ 450 ℃ in the entire photonics integration process.

Deposited photonics [12–14] was proposed for monolithic back-end integration on CMOS to avoid epitaxial growth. Back-end integrated PICs mainly rely on polycrystalline silicon (poly-Si) due to its capability for p/n doping and its high mobility of up to 100 $cm^2/V \cdot s$ [12], advantages that other deposited materials like amorphous silicon (α-Si) and silicon nitride (SiN) do not possess. Poly-Si was demonstrated for integrated optical modulators [13], photodetectors [15–16], gas sensing [17], and narrowband reflectors [18]. Meanwhile, poly-Si could also construct poly-Si/SiO_2/single-crystalline-Si MOS waveguide [19] to enhance the extinction ratio of a low-quality-factor, high-speed plasma-dispersion-effect ring modulators, or act as micro-heaters for CMOS photonics [20]. Another challenge for low-temperature deposited photonics is the high-temperature (>1000 °C) annealing required for implant activation. Excimer laser annealing (ELA) technology [21], utilized in the thin film transistor (TFT) industry, offers a potential solution. During ELA, nanosecond excimer laser pulses irradiating on the surface of α-Si thin film were absorbed and converted to heat, and the temperature can be high enough to crystallize the α-Si into poly-Si on glass substrates [22–23] and activate ion dopants inside [24–25]. Meanwhile, the limited penetration depth of UV laser and short pulse duration ensure minimal heat transfer to the underlying substrate, making it potentially suitable for back-end integrated PIC fabrication. Hence, similar laser annealing approaches were demonstrated in integrated photonics. For instance, Franz et al. [26] used a continuous-wave argon ion laser at 488 nm wavelength to anneal patterned α-Si waveguides, achieving a low propagation loss of 5.3 dB/cm. Lee et al. [13] utilized an excimer laser to crystallize an entire α-Si film and subsequently fabricated poly-Si optical modulators, achieving carrier injection modulation at 3 Gbps.

Nonetheless, the research on monolithic back-end integrated photonics and the application of laser annealing therein is still in its infancy, with key techniques in this area requiring further exploration. Due to the presence of grain boundaries, the optical loss in poly-Si waveguides is inevitably high, which is detrimental to the construction of large-scale links. In contrast, its amorphous counterpart, α-Si, exhibits a low optical loss, but its low mobility prevents it from constructing active devices. Notably, the characteristics of poly-Si and α-Si respectively correspond to the performance requirements of PICs' active and passive components. A potential breakthrough lies in how to leverage the advantages of both materials simultaneously to achieve high-performance deposited PICs.

In this paper, we propose an α-Si/poly-Si hybrid device structure to realize CMOS-back-end-of-line-compatible silicon-based optoelectronic integration with the help of laser annealing technique to locally crystalize the α-Si into poly-Si in the active region while maintaining its amorphous state in passive areas. To validate the key fabrication steps, we investigated the UV-laser crystallization of α-Si thin films with a thickness of a typical waveguide layer by employing a solid-state laser ($\lambda = 355$ nm) and an excimer laser ($\lambda = 308$ nm), respectively. The effect of pre-dehydrogenation, doping and thickness of α-Si thin films, pulse energy density, and pulse number of lasers were also studied. The dopant activation was validated by the ohmic contact between the metallic electrode pads and laser-crystallized heavily doped α-Si. We then verified the realization of mask-assisted local ELA, and the utilization of a SiO_2 spacer layer was emphasized. This technique can not only realize low-loss α-Si/poly-Si hybrid photonic devices but also make the high-yield wafer-level ELA on deposited PICs feasible.

2. α-Si/poly-Si hybrid structure for deposited photonics

Fig. 1 shows the 3D schematic diagram of the α-Si/poly-Si hybrid structure proposed for low-temperature and low-loss CMOS-back-end-of-line-compatible silicon-based optoelectronic integration. The α-Si ridge waveguides form the building block of the deposited PICs. By leveraging the local laser annealing technique, the α-Si can be laser-crystallized into poly-Si only in the active region. The doping profile takes the form of standard silicon photonics, and this basic structure can be embedded in resonators and interferometers as phase shifters or attenuators, further achieving optical switches, modulators, waveguide attenuators, and networks. This architecture allows for the utilization of the low optical loss of α-Si in passive components, while simultaneously taking advantage of the low resistance (and high mobility) of the poly-Si active regions.

3. Validation and discussions of key techniques

3.1. Laser-crystallization of α-Si thin films

1) Laser annealing on intrinsic α-Si.

It has been reported that laser annealing of α-Si thin films can be achieved using continuous-wave and pulsed lasers with wavelengths ranging from ultraviolet to near-infrared [27]. Due to the higher UV absorption rate of α-Si and its resultant superior crystallization effects, UV laser annealing was studied in this study, including solid-state laser annealing (SLA) with excimer laser annealing (ELA). The principle of laser crystallization of α-Si has been widely discussed in TFTs and display industry. Due to the relatively small penetration depth of the UV light in α-Si, the laser pulse with the energy density that exceeds a certain threshold would melt the top surface of an α-Si thin film, and the molten front would penetrate downwards [28]. After the laser pulse energy ceases, the molten material rapidly cools, and the original interface between the solid phase and the liquid phase moves back to the surface [29]. During this process, due to the presence of crystal seeds in

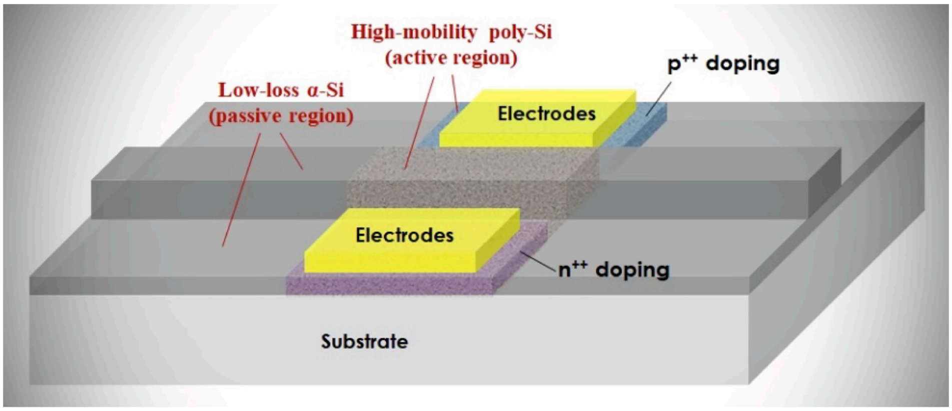

Fig. 1. A schematic diagram of the α-Si/poly-Si hybrid structure for deposited photonics.

the amorphous silicon, the softened silicon arranges itself according to the lattice structure on these crystal nuclei and forms poly-Si. With the increase of the laser energy density, the grain sizes first increase, reaching a maximum near the critical point of complete melting, and then decrease due to homogeneous nucleation [22]. Therefore, we start by optimizing the pulse energy density to achieve the crystallization of α-Si thin films, ensuring the energy density is maintained between the crystallization and ablation thresholds, and promoting the growth of larger grains. Large grains can decrease propagation loss and facilitate electronic transport by reducing grain boundaries in the waveguides and devices.

220 nm-thick α-Si thin films were grown by plasma-enhanced chemical vapor deposition (PECVD) on an 8-inch Si wafer with 2 μm-thick buried oxide (BOX) layer. Subsequently, SLA was realized by employing a UV pulse laser (Han's Laser Corporation, Draco Series) with an output wavelength of 355 nm, a repetition rate of 30 kHz, and a pulse width set to 20 ns. The Gaussian beam with a diameter of ~50 μm scans over the sample panel, controlled by a galvanometer mirror to manipulate the spot overlap, corresponding to the number of shots for each area. Fig. 2(a) shows the changes in Raman spectra of the 220-nm thick α-Si films after exposed to a single shot of laser pulse with various pulse energies. The crystallization threshold is speculated to be around 655 mJ/cm^2, according to the characteristic peak for crystalline Si(111) near 520 cm^{-1} in the Raman spectra. With the further increase of pulse

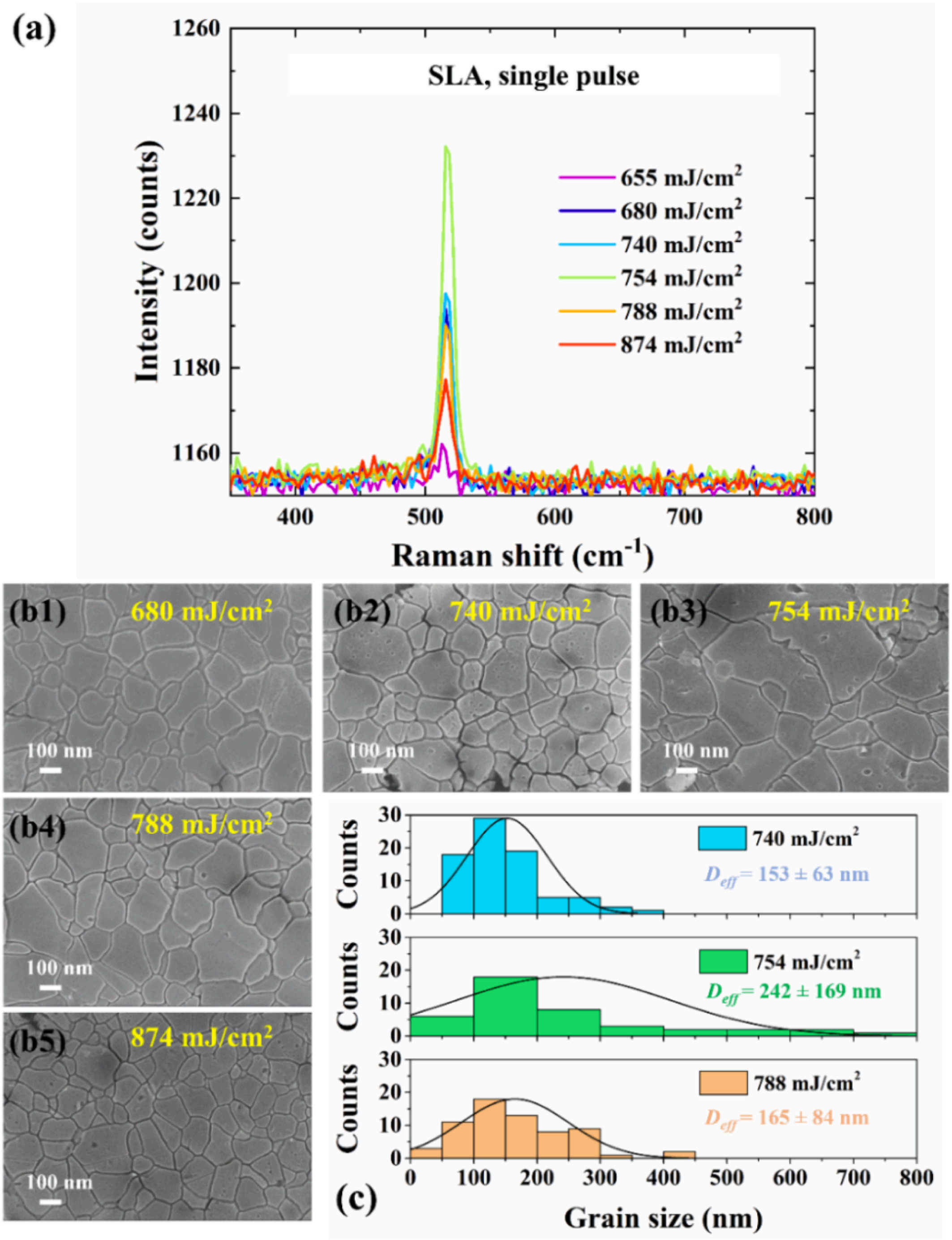

Fig. 2. Optimization of laser pulse energy density during SLA. (a) Raman spectra and (b1 ~ b5) SEM images of α-Si after single-pulse SLA with various pulse energies. (c) Statistically measured grain sizes according to SEM images.

energy density, the Raman peak intensity first increased and then decreased, suggesting a relatively better crystallinity around the single pulse energy density of 754 mJ/cm^2. A similar trend has been reported in ELA [30–31] and femtosecond laser annealing [32] process, and the turning point is considered to be related to super-lateral growth nucleation in the near-complete melting regime, featuring much larger grain sizes. This was confirmed by scanning electron microscope (SEM) images of laser-crystallized α-Si thin films, as shown in Fig. 2(b1) ~ (b5). All the samples were etched in SECCO solution to expose the grain boundaries. Fig. 2(c) shows the statistically measured effective grain sizes according to SEM images of laser-crystallized poly-Si films, and larger grains (with an average effective diameter of ~ 250 nm) appear in the poly-Si film crystallized by the laser pulse with a pulse energy density of 754 mJ/cm^2.

The pulse energy density for ELA was then optimized in the same way. A 308 nm-wavelength excimer laser (Shenzhen Shengfang Technology Co., Ltd, PLD series) with a pulse width of 25 ns was used, the repetition rate was set to 10 Hz, and the pulse energy density was set to ~ 270 mJ/cm^2. The spot size of the laser was 35 mm by 350 μm, and the laser beam arrived on the α-Si thin film was top-hat along the long axis and nearly top-hat along the short axis. Fig. 3(b1) shows the surface morphology of the excimer laser-crystallized poly-Si thin film after SECCO etching, and it contains more larger grains and also more smaller grains (<50 nm) compared with the SLA one shown in Fig. 3(a1). However, ELA and SLA on as-grown α-Si thin films both lead to holes and voids. This film damage was caused by the explosive release of hydrogen in the PECVD α-Si thin film [33]. As a result, the α-Si thin film has to be dehydrogenated before laser annealing.

Dehydrogenation of α-Si thin film was conducted by annealing the film in an N_2 atmosphere at 450 ℃ for 3 h, and the following laser crystallization achieved significantly improved morphology, as shown in Fig. 3(a2) and (b2). Meanwhile, multi-pulse ELA after dehydrogenation realized much larger grains than SLA. This could be attributed to the reduction of defects caused by dehydrogenation, the higher tendency of ELA to induce explosive crystallization, and the multi-pulse-prompted crystal growth. No obvious amorphous/polycrystalline layering was observed in the cross-section (not shown), but thinner α-Si thin films are preferred to guarantee full crystallization. Fig. 3(c) shows the Raman spectra of as-deposited α-Si thin films and dehydrogenated α-Si after ELA. Laser crystallization of α-Si was verified by the disappearance of the broad peak of α-Si at ~ 480 cm^{-1} and the formation of the characteristic peak of poly-Si at ~ 520 cm^{-1}. Additionally, the intensity of the crystallization characteristic peak increased with the number of pulses.

2) Laser annealing on doped α-Si.

Besides intrinsic α-Si, the laser crystallization of doped Si is also critical to deposited active photonics. The laser crystallization must be done after doping for dopant activation and to avoid re-amorphization [34] during the high-energy doping process. Here, α-Si thin films were heavily p-doped (p^{++}) and n-doped (n^{++}) by boron (B) and phosphorus (P), respectively, fabricated in the IMECAS foundry. The X-ray photoelectron spectroscopy (XPS) depth profile of the doped α-Si thin films (see Fig. 4) shows a uniform doping concentration, and the doping concentration was calculated to be around 1.75×10^{22} cm^{-3} and 5×10^{21} cm^{-3} for p^{++}- and n^{++}-α-Si, respectively.

It is worth noticing that the thickness of the α-Si thin films has a significant effect on the grain size of laser-crystallized poly-Si. Applying SLA to a dehydrogenated n^{++} α-Si film etched to a thickness of 120 nm resulted in a larger grain size than a film with a thickness of 220 nm, as the surface morphology shows in Fig. 5(a) and (b). This is attributed to more nucleation centers in thicker films, as well as the higher energy needed for explosive crystallization of α-Si with a larger volume. Therefore, electrode contact in the heavily doped slab region of the ridge waveguide might be more beneficial than in the 220 nm-thick region.

However, SLA here led to partial crystallization-like Raman spectra, as shown in Fig. 5(a) and (b), even if the pulse energy density was increased to near the ablation threshold. Although the increase in pulse number might improve the crystallization quality, we did not obtain laser-crystallized poly-Si with good quality via SLA on heavily doped α-Si thin films. The precise reasons for this still need further investigation.

In contrast, ELA achieved better crystallinity for heavily doped α-Si, as suggested by the Raman spectra shown in Fig. 6. Hence, ELA is considered to be a better approach than SLA here for active photonic devices, since amorphous clusters resulted from insufficient crystallinity in SLA could lead to poor electronic transportation. Hence, ELA was adopted in the following study.

3.2. Activation of doping ions for ohmic contact

Optoelectronic devices involving electro-optical and opto-electrical conversion essentially require ohmic contact between electrodes and doped Si slabs. For CMOS-back-end deposited photonics, this asks for not only the aforementioned crystallization of α-Si, but also the low-temperature activation of dopants. Resistors as shown in Fig. 7(a) for instance were fabricated. ELA was first performed on the dehydrogenated 220 nm-thick heavily-doped α-Si thin films, where the laser

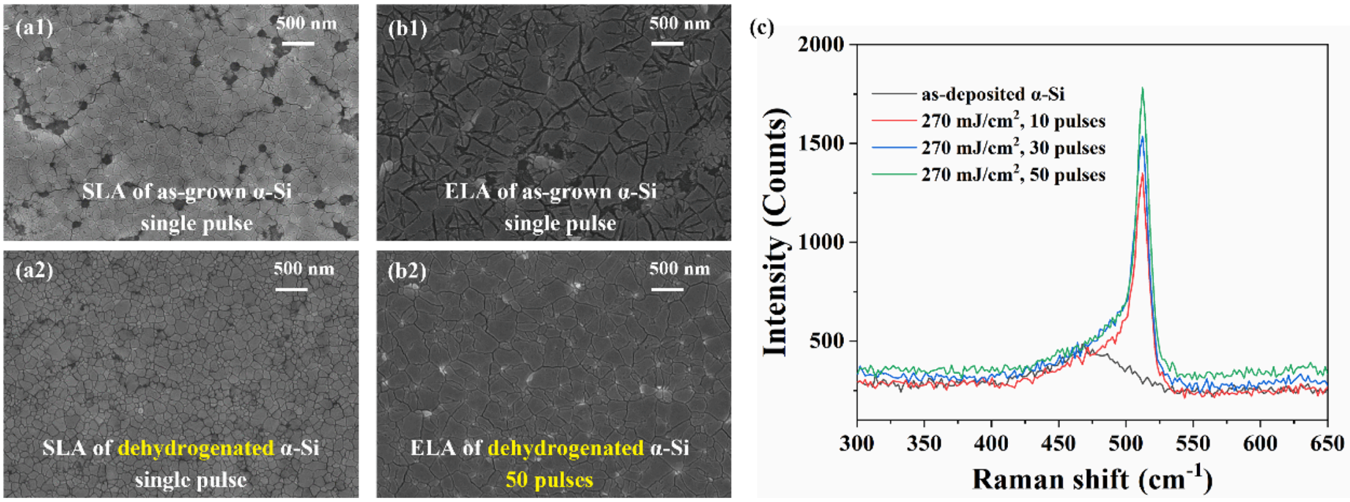

Fig. 3. The effect of α-Si pre-dehydrogenation and laser pulse number of SLA and ELA on the surface morphology: SEM images of (a1) as-grown and (a2) dehydrogenated α-Si after single-pulse SLA. SEM images of (b1) as-grown α-Si after 5-pulse ELA and (b2) dehydrogenated α-Si after 250-pulses ELA. (c) Raman spectra of dehydrogenated α-Si after multi-pulses ELA.

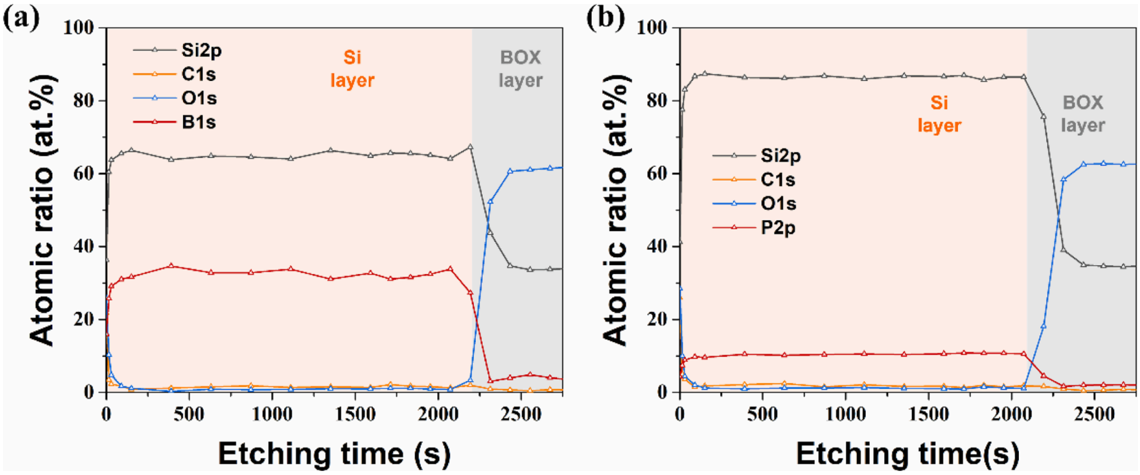

Fig. 4. XPS depth profile of doped α-Si thin films, including the substrate, showing the atomic ratio of dopants along the thickness direction for (a) p^{++} and (b) n^{++} α-Si.

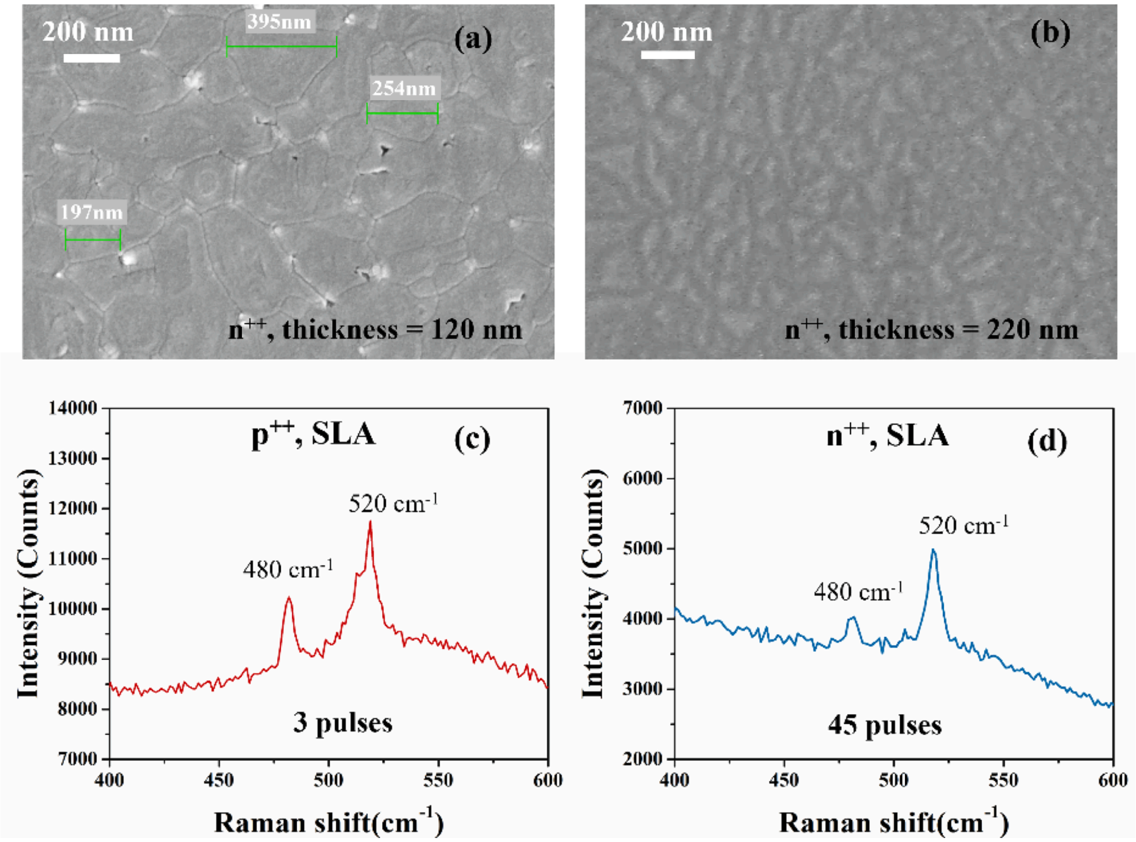

Fig. 5. SEM images of (a) 120 nm-thick and (b) 220 nm-thick n^{++}-*α*-Si after 60-pulse SLA with the same pulse energy density. Raman spectra of 220 nm-thick dehydrogenated (c) p^{++}-*α*-Si after 3-pulse SLA and (d) n^{++}-*α*-Si after 45-pulse SLA.

pulse energy density was 270 mJ/cm^2 and the pulse number was 50. Then, the pattern of the resistive strip was defined by UV lithography, and the laser-crystallized poly-Si was fully etched by inductively coupled plasma (ICP) etching. Finally, Al electrode pads were fabricated by UV lithography (UVL), e-beam evaporation, and lift-off process. Ti(5 nm)/Au(100 nm) electrodes also work according to our experiments.

To evaluate the resistivity of the laser-crystallized poly-Si, I-V curves of three devices on each chip were randomly measured. The linear dependence of current on voltage demonstrates good ohmic contact between the metal electrode and the heavily doped amorphous silicon treated with ELA, as shown in Fig. 7 (b) and (c) for p^{++} and n^{++} ones, respectively. This validated the activation of dopants during ELA crystallization. The resistivity of ELA-crystallized p^{++}-poly-Si was calculated to be 7.49E-4 ± 4.22E-5 Ω·cm, and the resistivity of its n^{++} counterpart was calculated to be 1.39E-3 ± 3.3 × E-4 Ω·cm, which is larger due to the lower doping concentration. However, it has to be noted that the electrical properties vary to some extent among devices, especially for films with a lower doping concentration. This may be attributed to the nonuniformity of laser exposure due to the overlap between spots during scanning in ELA. Therefore, an excimer laser annealing system with a

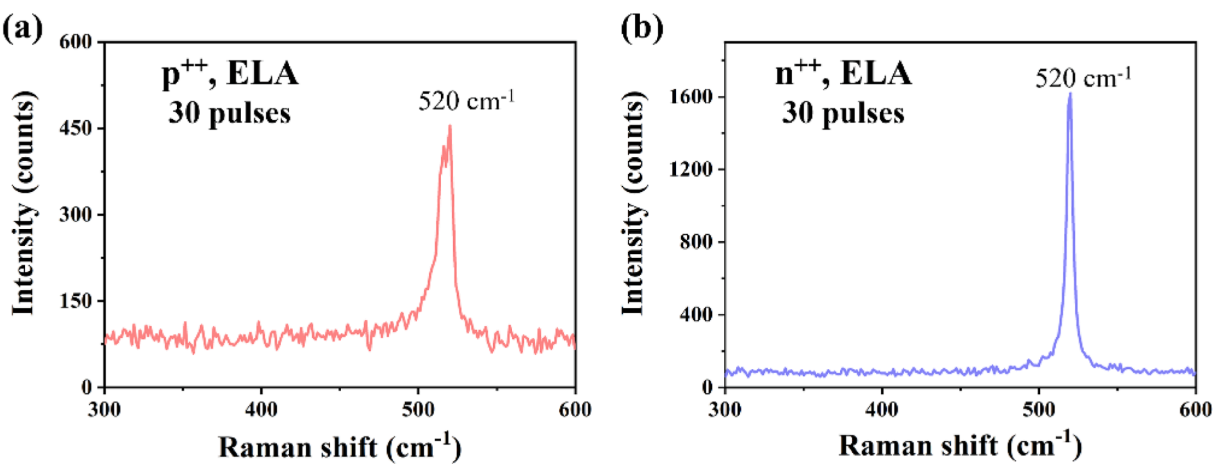

Fig. 6. Raman spectra of dehydrogenated heavily doped (a) p^{++} and (b) n^{++} α-Si after ELA.

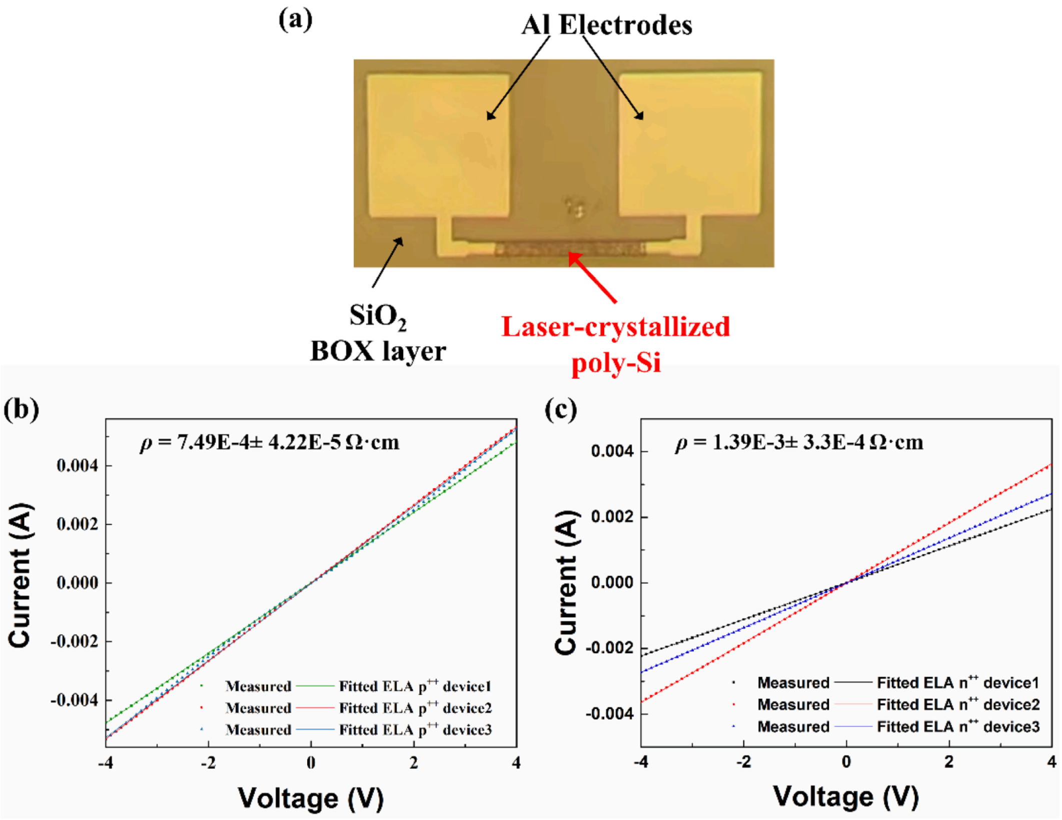

Fig. 7. Ohmic contact between metallic electrodes and excimer-laser annealed α-Si. (a) An optical micrograph of the device used for the measurement of resistivity of α-Si after ELA. I-V curves of the (b) p^{++} and (c) n^{++} excimer-laser crystallized poly-Si resistors.

line beam that covers the wafer in one direction is preferred for deposited photonics.

3.3. Metallic mask-assisted ELA for low-loss α-Si/poly-Si hybrid devices

Whether it is to improve yield in large-scale integration or to ensure uniformity in ELA, large spot or line beam scanning is necessary. However, the loss caused by the crystallization of α-Si sheets cannot be ignored in deposited photonics. Therefore, mask-assisted ELA, which covers areas such as grating couplers and passive components and exposes the active region only, is essential.

Al(200 nm-thick) [35] or Al(150 nm)/Cr(50 nm) [33] masks covering on α-Si have been used in ELA study for TFTs. For instance, utilizing the shading and thermal conductivity properties of the metallic masks, ELA could induce lateral thermal gradients within the Si film, thereby inducing super-lateral growth (SLG) in a 2 μm-wide exposed gap and forming ~ 1 μm-wide oriented large grains with a single boundary at the center of the gap [35]. Although in photonic devices the active regions are much wider than the exposed gap of the Al mask in previously reported studies (2 μm) for TFTs thus the mask-induced SLG may not occur, shading the passive components of PICs could still be realized via an ELA mask.

However, directly transitioning from mask-assisted ELA in TFT studies to photonic devices- that is, covering an Al mask on α-Si (as shown in Fig. 8(c)) and removing it after ELA- was found to result in ultra-high propagation loss in photonic devices. Fig. 8(d) shows an SEM

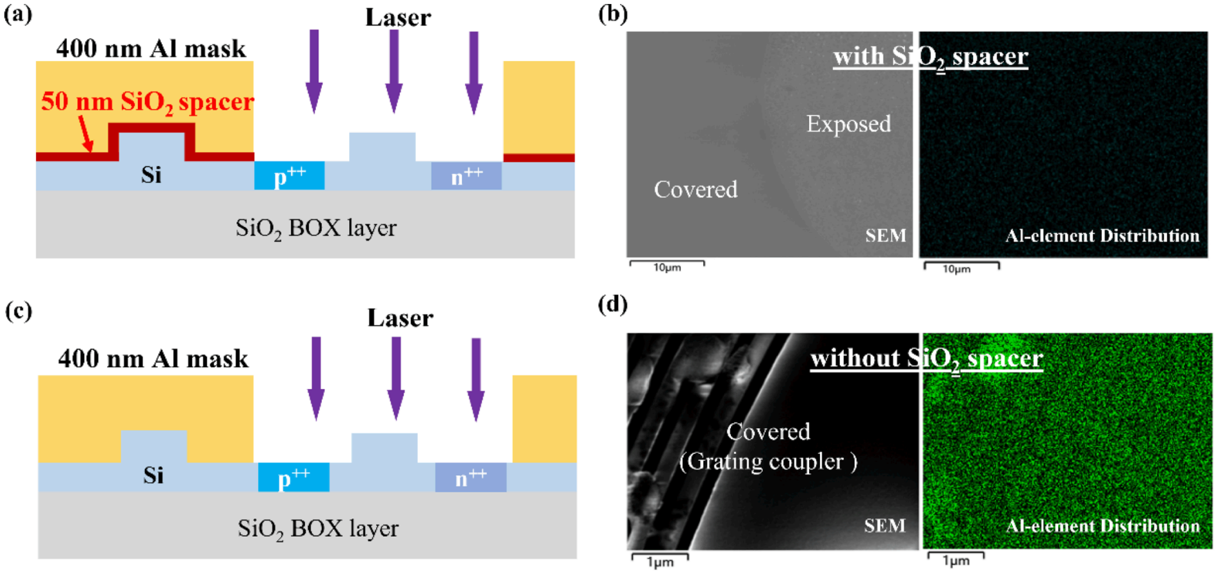

Fig. 8. The effect of silica spacer layer on Al mask-assisted ELA: schematic diagram of the cross-section of the Al mask-assisted ELA on photonic devices (a) with and (c) without the silica spacer layer. SEM images and EDS mapping of α-Si photonic devices after Al mask-assisted ELA (b) with and (c) without the spacer. The Al mask and silica buffer layer were removed before characterization.

image and the corresponding energy dispersive spectroscopy (EDS) mapping of a mask-covered grating coupler after removing the mask, and the metal contamination was revealed. This contamination could be attributed to diffusion during local high-temperature ELA or/and residuals from wet etching.

Therefore, here we emphasize the utilization of a buffer layer between the Al mask and α-Si, as shown in Fig. 8(a). A layer of 50 nm-thick PECVD silica spacer was deposited onto dehydrogenated α-Si photonic structures before the Al mask was fabricated, and the SiO_2 in the window was removed before ELA. After ELA, the Al mask and the SiO_2 buffer layer were then removed. The SEM image in Fig. 8(b) shows the morphology of the covered and exposed area on α-Si after ELA and mask removal, where the boundary between α-Si and laser-crystallized poly-Si could be seen. The corresponding EDS mapping shows minimal presence of Al. Hence, the SiO_2 buffer layer needs to be at least 50 nm thick. Apart from the Al mask, other masks made from refractory metals like Ni and W with the same film thickness were also examined; however, the latter ones exhibited varying degrees of burning during the ELA process (not shown in the images).

The effectiveness of the aforementioned mask-shaded technique was further verified by applying it to α-Si grating couplers that connected to straight waveguides. The devices were fabricated on 220 nm-thick α-Si thin films with an etching depth of 150 nm on a 200 mm wafer in the IMECAS foundry. Fig. 9 (a) shows the transmittance spectra of a pair of grating couplers (connected by a 700 μm-long straight waveguide) on 3 different dies for comparison. The one on Die 1 was as-fabricated without any treatment, and the one on Die 2 underwent ELA crystallization without a mask (pulse number equals 50, and pulse energy density approximates 270 mJ/cm^2). It could be seen that the ELA crystallization lead to a significant decrease of coupling efficiency, which is due to the refraction and scattering loss caused by grain boundaries. On the contrary, the grating coupler on Die 3 was completely masked during the ELA process (i.e. not exposed to the laser), and the coupling efficiency is very close to the as-fabricated one. This manifests that the ELA mask effectively prevents the passive components from laser annealing.

Similar experiments were conducted on racetrack resonators to assess the mask-assisted local ELA on photonic devices, and the

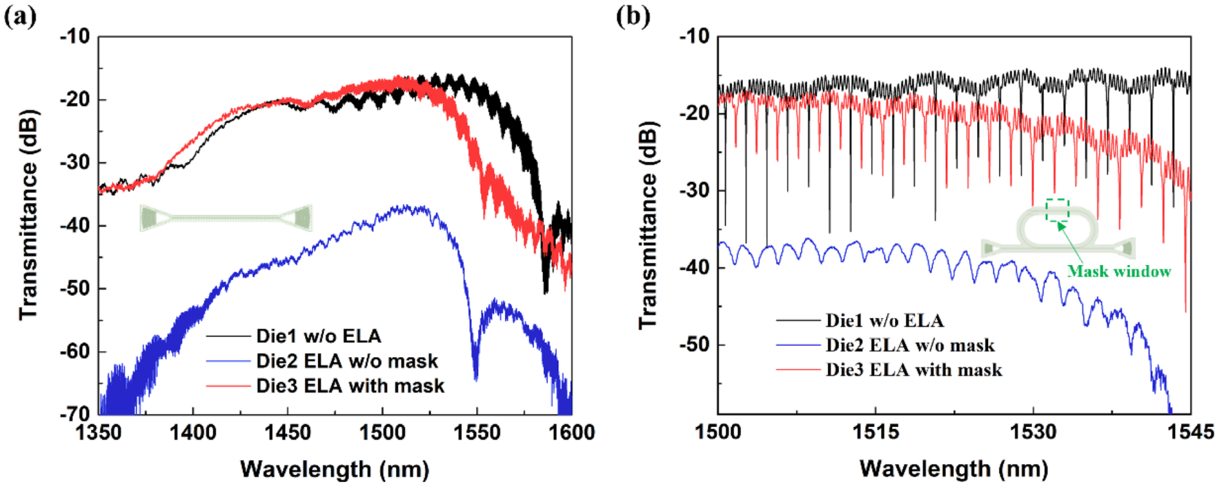

Fig. 9. Mask-assisted local ELA for low loss deposited photonic devices: Transmittance spectra of (a) grating couplers and (b) racetrack resonators with and without metallic mask. The devices were fabricated on different dies of an 8-inch wafer. The insets show schematic diagrams of the devices.

transmittance spectra are shown in Fig. 9 (b). The only difference from the previous grating coupler experiments is that, in the mask-assisted local ELA on Die3, a 20 μm-long window was opened on the waveguide of the resonator instead of completely covering the entire device. Note that the window length of 20 μm was chosen as an example to mimic a typical length of the active region of an optical switch or modulator. The racetrack resonators had a perimeter of ~ 187 μm and a coupling gap of 300 nm, and the as-fabricated resonator was near its critical coupling state, exhibiting a *Q* factor of ~ 15,000 and an extinction ratio (ER) of ~ 15 dB. After ELA without shading mask, the coupling loss of the grating couplers connected to the bus waveguide increased by ~ 20 dB, and the *Q* factor decreased to ~ 1,800 with an ER of ~ 4 dB. Correspondingly, the waveguide propagation loss increased from ~ 22 dB/cm (α-Si) to ~ 200 dB/cm (poly-Si) after ELA of a resonator without a mask, which was extracted from the resonator transmittance spectra using the coupled wave transfer matrix method [36]. In contrast, the racetrack resonator which underwent mask-assisted ELA with only a section of 20 μm-long waveguide in the resonator exposed was measured to present a *Q* factor of ~ 8,000 and ER of ~ 10 dB. The propagation loss in the resonator was calculated to be around 60 dB/cm. This propagation loss is obviously lower than in the case without an ELA mask but is higher than expected. The excess loss is attributed to a small quantity of Al residuals during the removal of ELA mask using tribasic acid (as shown in Fig. 8(b)), and could be eliminated by optimization of the metal removal recipe.

Based on the assessment of waveguide propagation loss, the change of the coupling loss of the bare grating couplers (without the connecting waveguide) before and after ELA could be obtained by deducting the waveguide loss from the transmittance of the whole device shown in Fig. 9(a). After unmasked ELA, the coupling loss of the as-fabricated α-Si grating couplers increased from 15 dB/pair to 23 dB/pair at a wavelength of 1525 nm. This indicates that the Al mask effectively prevented an 8 dB/pair increase in coupling loss due to ELA-induced crystallization in the α-Si grating couplers.

4. Fabrication flow of the *α*-Si/poly-Si hybrid photonic devices

Based on the experiments and validations, we propose the fabrication flow of the *α*-Si/poly-Si hybrid deposited photonics on CMOS as shown in Fig. 10. It starts with a CMOS wafer with a metal interconnection redistribution layer (RDL). First, a 2 μm-thick SiO_2 dielectric layer is deposited by PECVD, and W/Al vias were fabricated. Next, a 220 nm-thick *α*-Si thin film is deposited by PECVD and patterned to form photonic structures. The active region is sequentially doped with low, medium (if necessary), and high concentrations. Dehydrogenation of *α*-Si thin film can be conducted at this time by annealing at 450 °C for 3 h in an N_2 atmosphere. Following this, a SiO_2 buffer layer no less than 50 nm thickness is deposited by PECVD. A 400 nm-thick Al thin film is then e-beam evaporated and liftoff after the mask pattern is defined by UVL. Afterward, the SiO_2 buffer on the active region (within the mask window) is removed via ICP etching followed by hydrofluoric acid (HF) wet etching. Multi-pulse ELA with a pulse energy density of ~ 270 mJ/cm^2 is applied to crystallize the entire active region and activate the dopants simultaneously. Alternatively, the mask fabrication and ELA process can be repeated multiple times to anneal the intrinsic and doped regions separately with optimized pulse energy density lasers. Subsequently, the Al mask could be removed by tribasic acid ($H_3PO_4 + HNO_3 + CH_3COOH$) first, and the SiO_2 buffer layer can be removed by HF. Finally, the SiO_2 upper cladding is deposited by PECVD.

5. Conclusion

In this paper, we proposed an *α*-Si/poly-Si hybrid structure for low-temperature deposited silicon photonics on CMOS to leverage both the low propagation loss of *α*-Si waveguides and the high mobility of poly-Si. This approach relies on the mask-assisted local laser crystallization of *α*-Si in the active regions. Compared to solid-state lasers, excimer lasers achieved higher-performance laser crystallization of α-Si, as indicated by the better crystallinity of doped α-Si and improved surface morphology. Thinner α-Si films tend to form larger crystals than thicker ones, suggesting that electrode contact in the heavily doped slab region of the ridge waveguide might be more beneficial. Furthermore, the ELA on doped *α*-Si thin films can simultaneously achieve crystallization of *α*-Si and the activation of doping ions, as verified by the ohmic contact between the metallic electrode pads and heavily doped *α*-Si after ELA. The resistivity of ELA-crystallized poly-Si with a boron doping concentration of 1.75 × 10 [22] cm^{-3} was measured to be around 7.49E-4 Ω·cm, and the resistivity of its n^{++} counterpart with a phosphorus doping concentration of 5 × 10 [21] cm^{-3} was 1.39E-3 Ω·cm. We also validated that the mask-assisted local ELA, which exposes the active

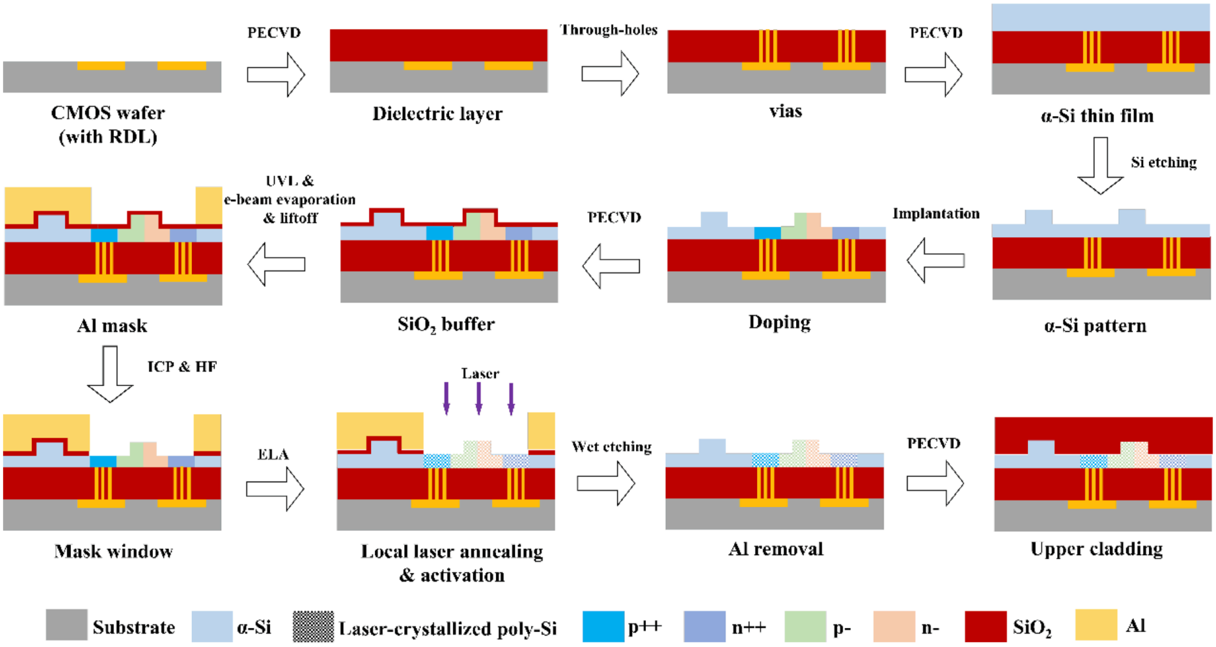

Fig. 10. A schematic diagram of the suggested fabrication flow of the *α*-Si/poly-Si hybrid deposited photonic devices on CMOS.

functional area only and covers up the passive components in PICs, not only makes the high-yield wafer-level ELA feasible but also prevents the increase of optical loss in waveguides by ∼ 140 dB/cm and coupling loss in grating couplers by ∼ 8 dB/pair. Based on the experimental validation of these key techniques, we proposed a fabrication flow of the α-Si/poly-Si hybrid photonics for low-temperature deposited silicon photonics on CMOS. Building on the experiments and device structures presented in this paper, further optimization can be achieved, for instance, by incorporating SiN to reduce losses and decreasing the α-Si thickness to enable better laser crystallization. This work may provide valuable references and new insights for back-end deposited photonics.

CRediT authorship contribution statement

Junying Li: Writing – review & editing, Writing – original draft, Supervision, Methodology, Investigation, Funding acquisition, Conceptualization. **Lichun Wang:** Writing – review & editing, Investigation. **Xinru Xu:** Writing – review & editing, Investigation, Data curation. **Kunhao Lei:** Writing – review & editing, Writing – original draft, Investigation, Data curation. **Bo Tang:** Writing – review & editing, Investigation. **Hao Dai:** Writing – review & editing, Investigation. **Jiaxin Zhang:** Writing – review & editing, Investigation. **Jialing Jian:** Writing – review & editing, Investigation. **Yuting Ye:** Writing – review & editing, Investigation. **Hui Ma:** Writing – review & editing, Investigation. **Jianghong Wu:** Writing – review & editing, Investigation. **Ye Luo:** Writing – review & editing, Investigation. **Zequn Chen:** Writing – review & editing, Investigation. **Yuexin Yin:** Writing – review & editing, Investigation. **Chunlei Sun:** Writing – review & editing, Investigation. **Daming Zhang:** Writing – review & editing, Supervision. **Lan Li:** Writing – review & editing, Supervision, Funding acquisition. **Hongtao Lin:** Writing – review & editing, Supervision, Methodology, Funding acquisition, Conceptualization.

Declaration of competing interest

The authors declare that they have no known competing financial interests or personal relationships that could have appeared to influence the work reported in this paper.

Data availability

Data will be made available on request.

Acknowledgments

This work was supported by the National Natural Science Foundation of China (62105287), the National Key Research & Development Program of China (2021YFB2801300 and 2019YFB2203002), Zhejiang Provincial Natural Science Foundation of China (LD22F040002), and the Research Funds of Hangzhou Institute for Advanced Study, UCAS (2023HIAS-Y001). The authors would like to acknowledge the fabrication and characterization support from the ZJU Nano-Fabrication Center at Zhejiang University, Institute of Microelectronics of the Chinese Academy of Sciences, and Shenzhen Shengfang Technology Co., Ltd. The authors thank Dr. Zhong Chen and Dr. Pei Sheng from Instrumentation and Service Center for Physical Sciences and Molecular Sciences at Westlake University for supporting the Raman and XPS characterization.

References

[1] S. Shekhar, et al., Roadmapping the next generation of silicon photonics, Nat. Commun. 15 (2024), https://doi.org/10.1038/s41467-024-44750-0.
[2] A.H. Ahmed, et al. in 2019 IEEE International Solid-State Circuits Conference - (ISSCC). 484-486.
[3] X. Zhang, K. Kwon, J. Henriksson, J. Luo, M.C. Wu, A large-scale microelectromechanical-systems-based silicon photonics LiDAR, Nature 603 (2022) 253–258, https://doi.org/10.1038/s41586-022-04415-8.
[4] F. Ashtiani, A.J. Geers, F. Aflatouni, An on-chip photonic deep neural network for image classification, Nature 606 (2022) 501–506, https://doi.org/10.1038/s41586-022-04714-0.
[5] W. Bogaerts, et al., Programmable photonic circuits, Nature 586 (2020) 207–216, https://doi.org/10.1038/s41586-020-2764-0.
[6] B.D. Reed, et al., Real-time dynamic single-molecule protein sequencing on an integrated semiconductor device, Science 378 (2022) 186–192, https://doi.org/10.1126/science.abo7651.
[7] V. Stojanović, et al., Monolithic silicon-photonic platforms in state-of-the-art CMOS SOI processes [Invited], Opt. Express 26 (2018), https://doi.org/10.1364/oe.26.013106.
[8] A.H. Atabaki, et al., Integrating photonics with silicon nanoelectronics for the next generation of systems on a chip, Nature 556 (2018) 349–354, https://doi.org/10.1038/s41586-018-0028-z.
[9] S. Meister, et al. Silicon photonics for 100 Gbit/s intra-data center optical interconnects. Vol. 9753 PWO (SPIE, 2016).
[10] D. Shin, et al., Bulk-Si Platform: Born for DRAM, Upgraded With On-Chip Lasers, and Transplanted to LiDAR, J. Lightwave Technol. 40 (2022) 3137–3148.
[11] A. Li, et al., A 256 Gb/s electronic−photonic monolithically integrated transceiver in 45 nm CMOS, J. Semicond. 45 (2024), https://doi.org/10.1088/1674-4926/24050040.
[12] Y.H.D. Lee, M. Lipson, Back-End Deposited Silicon Photonics for Monolithic Integration on CMOS, IEEE J. Sel. Top. Quantum Electron. 19 (2013) 8200207, https://doi.org/10.1109/jstqe.2012.2209865.
[13] Y.H.D. Lee, M.O. Thompson, M. Lipson, Deposited low temperature silicon GHz modulator, Opt. Express 21 (2013), https://doi.org/10.1364/oe.21.026688.
[14] J. Fujikata, M. Takahashi, S. Takahashi, T. Horikawa, T. Nakamura, High-speed and high-efficiency Si optical modulator with MOS junction, using solid-phase crystallization of polycrystalline silicon, Jpn. J. Appl. Phys. 55 (2016), https://doi.org/10.7567/jjap.55.042202.
[15] A.H. Atabaki, H. Meng, L. Alloatti, K.K. Mehta, R.J. Ram, High-speed polysilicon CMOS photodetector for telecom and datacom, Appl. Phys. Lett. 109 (2016), https://doi.org/10.1063/1.4962641.
[16] K.K. Mehta, et al., Polycrystalline silicon ring resonator photodiodes in a bulk complementary metal-oxide-semiconductor process, Opt. Lett. 39 (2014), https://doi.org/10.1364/ol.39.001061.
[17] C. Consani, et al., Mid-infrared photonic gas sensing using a silicon waveguide and an integrated emitter, Sens. Actuators B 274 (2018) 60–65, https://doi.org/10.1016/j.snb.2018.07.096.
[18] Y. Hung Jr., et al., Low-loss polysilicon subwavelength grating waveguides and narrowband Bragg reflectors in bulk CMOS, Opt. Express 28 (2020), https://doi.org/10.1364/oe.381894.
[19] W. Zhang, et al., Harnessing plasma absorption in silicon MOS ring modulators, Nat. Photonics 17 (2023) 273–279, https://doi.org/10.1038/s41566-023-01159-3.
[20] R.M. Krishna, et al., Polysilicon micro-heaters for resonance tuning in CMOS photonics, Opt. Lett. 47 (2022), https://doi.org/10.1364/ol.441510.
[21] N. Matsuo, A. Heya, H. Hamada, Review—Technology Trends of Poly-Si TFTs from the Viewpoints of Crystallization and Device Performance, ECS J. Solid State Sci. Technol. 8 (2019) P239–P252, https://doi.org/10.1149/2.0211903jss.
[22] L. Mariucci, A. Pecora, G. Fortunato, C. Spinella, C. Bongiorno, Crystallization mechanisms in laser irradiated thin amorphous silicon films, Thin Solid Films 427 (2003) 91–95, https://doi.org/10.1016/s0040-6090(02)01254-3.
[23] C.T. Angelis, et al., Effect of excimer laser annealing on the structural and electrical properties of polycrystalline silicon thin-film transistors, J. Appl. Phys. 86 (1999) 4600–4606, https://doi.org/10.1063/1.371409.
[24] G. Fortunato, et al., Electrical activation phenomena induced by excimer laser annealingin B-implanted silicon, Appl. Phys. Lett. 85 (2004) 2268–2270, https://doi.org/10.1063/1.1793352.
[25] S. Whelan, et al., Dopant redistribution and electrical activation in silicon following ultra-low energy boron implantation and excimer laser annealing, Phys. Rev. B 67 (2003), https://doi.org/10.1103/PhysRevB.67.075201.
[26] Y. Franz, et al., Laser crystallized low-loss polycrystalline silicon waveguides, Opt. Express 27 (2019), https://doi.org/10.1364/oe.27.004462.
[27] D. Arduino, et al., Silicon and Silicon Carbide Recrystallization by Laser Annealing: A Review, Materials 16 (2023), https://doi.org/10.3390/ma16247674.
[28] K.A. Jackson, in Surface Modification and Alloying: by Laser, Ion, and Electron Beams (eds J. M. Poate, G. Foti, & D. C. Jacobson) 51-79 (Springer US, 1983).
[29] H. Kuriyama, et al., Enlargement of Poly-Si Film Grain Size by Excimer Laser Annealing and Its Application to High-Performance Poly-Si Thin Film Transistor, Jpn. J. Appl. Phys. 30 (1991) 3700, https://doi.org/10.1143/JJAP.30.3700.
[30] C.-C. Kuo, W.-C. Yeh, J.-F. Lee, J.-Y. Jeng, In-Situ and Ex-Situ Measurements on Silicon Thin Films Fabricated by Excimer Laser Annealing, J. Phys. Conf. Ser. 48 (2006) 937–944, https://doi.org/10.1088/1742-6596/48/1/177.
[31] J.S. Im, H.J. Kim, M.O. Thompson, Phase transformation mechanisms involved in excimer laser crystallization of amorphous silicon films, Appl. Phys. Lett. 63 (1993) 1969–1971, https://doi.org/10.1063/1.110617.
[32] J.-M. Shieh, et al., Near-infrared femtosecond laser-induced crystallization of amorphous silicon, Appl. Phys. Lett. 85 (2004) 1232–1234, https://doi.org/10.1063/1.1782267.
[33] S. Loreti, D. della Sala, M. Garozzo, Morphological and structural effects of excimer laser treatment of amorphous silicon, Micron 31 (2000) 299–307, https://doi.org/10.1016/S0968-4328(99)00097-9.

[34] T. Sameshima, N. Andoh, Y. Andoh, Activation Behavior of Boron and Phosphorus Atoms Implanted in Polycrystalline Silicon Films by Heat Treatment at 250°C, Jpn. J. Appl. Phys. 44 (2005) 1186, https://doi.org/10.1143/JJAP.44.1186.

[35] J. Jae-Hong, L. Min-Cheol, P. Kee-Chan, H. Min-Koo, A new polycrystalline silicon TFT with a single grain boundary in the channel, IEEE Electron Device Lett. 22 (2001) 429–431, https://doi.org/10.1109/55.944329.

[36] A. Yariv, Universal relations for coupling of optical power between microresonators and dielectric waveguides, Electron. Lett. 36 (2000) 321–322, https://doi.org/10.1049/el:20000340.